

Article

Covalently Bonded Ir(IV) on Conducted Blue TiO₂ for Efficient Electrocatalytic Oxygen Evolution Reaction in Acid Media

Chau T. K. Nguyen ^{1,2,†}, Ngoc Quang Tran ^{1,†}, Thi Anh Le ^{1,2} and Hyoyoung Lee ^{1,2,3,4,*} 

¹ Center for Integrated Nanostructure Physics, Institute for Basic Science (IBS), Sungkyunkwan University, Suwon 16419, Korea; ntkchau92@gmail.com (C.T.K.N.); tnquang@hcmus.edu.vn (N.Q.T.); leanhmse@gmail.com (T.A.L.)

² Department of Chemistry, Sungkyunkwan University, Suwon 16419, Korea

³ Department of Biophysics, Sungkyunkwan University, Suwon 16419, Korea

⁴ Creative Research Institute, Sungkyunkwan University, Suwon 16419, Korea

* Correspondence: hyoyoung@skku.edu

† Contribute equally to this work.

Abstract: The stability of anode electrode has been a primary obstacle for the oxygen evolution reaction (OER) in acid media. We design Ir-oxygen of hydroxyl-rich blue TiO₂ through covalent bonds (Ir–O₂–2Ti) and investigate the outcome of favored exposure of different amounts of covalent Ir–oxygen linked to the conductive blue TiO₂ in the acidic OER. The Ir-oxygen-blue TiO₂ nanoclusters show a strong synergy in terms of improved conductivity and tiny amount usage of Ir by using blue TiO₂ supporter, and enhanced stability using covalent Ir-oxygen-linking (i.e., Ir oxide) in acid media, leading to high acidic OER performance with a current density of 10 mA cm^{−2} at an overpotential of 342 mV, which is much higher than that of IrO₂ at 438 mV in 0.1 M HClO₄ electrolyte. Notably, the Ir–O₂–2Ti has a great mass activity of 1.38 A/mg_{Ir} at an overpotential 350 mV, which is almost 27 times higher than the mass activity of IrO₂ at the same overpotential. Therefore, our work provides some insight into non-costly, highly enhanced, and stable electrocatalysts for the OER in acid media.

Keywords: acidic OER; blue TiO₂; iridium nanoclusters; mass activity



Citation: Nguyen, C.T.K.; Tran, N.Q.; Le, T.A.; Lee, H. Covalently Bonded Ir(IV) on Conducted Blue TiO₂ for Efficient Electrocatalytic Oxygen Evolution Reaction in Acid Media. *Catalysts* **2021**, *11*, 1176. <https://doi.org/10.3390/catal11101176>

Academic Editor: Nicolas Alonso-Vante

Received: 3 September 2021

Accepted: 27 September 2021

Published: 28 September 2021

Publisher's Note: MDPI stays neutral with regard to jurisdictional claims in published maps and institutional affiliations.



Copyright: © 2021 by the authors. Licensee MDPI, Basel, Switzerland. This article is an open access article distributed under the terms and conditions of the Creative Commons Attribution (CC BY) license (<https://creativecommons.org/licenses/by/4.0/>).

1. Introduction

Solar and wind powers are encouraging electricity production technologies for promoting a renewable and clean energy organization. Unfortunately, the discontinuous convenience of solar and wind powers critically encumber their wide variety of applications. Therefore, efficient and accessible means for storing energy are demanded to bridge the gap between supply and requirement [1,2]. Hydrogen (H₂) generated from the electrocatalytic water splitting (EWS) could feed such a long-time energy storage system due to the high density of gravimetric energy. The EWS is an important step for reaching renewable H₂ energy storage. However, the oxygen evolution reaction (OER), as one of the half-reactions in EWS, is a complicated transfer reaction of multi-electron, which includes a high overpotential to the actual reactive route, leading to a significant reduction of the reaction performance [3,4].

In the context of the EWS for renewable energy storage, the proton exchange membrane (PEM) electrolyzers possess more recognizable advantages than alkaline electrolyzers due to their limitation of gas boundary, high flexibility and great proton conductivity [5]. However, the main deficiency of the EWS system is that PEMs have driven in acidic media, which limit the series of materials available for the electrocatalytic anode parts and other auxiliaries such as current collectors and separators due to the maintaining high activity and stability required to these materials while the corrosion in acidic media was simultaneously resistance [6].

One possible approach to solving the catalyst problem is to apply nano-sized catalysts that are highly dissolved on the supporting materials with typical large sizes [7–9]. For the

supporting materials, long-term stability of the OER under acidic environments is necessary. For example, TiO_2 , SnO_2 , SiO_2 , silicon carbide-silicon and titanium carbide, among others, have been tested as supporting materials for noble-metal catalysts for the OER [10–12]. It is generally believed that reduced TiO_2 nanomaterials have properties proportional to the electrical conductivity, which is significantly improved by forming oxygen vacancies (V_{O}). A positive charge, then, Ti^{3+} from the center shifts away from the V_{O} position, leading to greatly enhanced electrocatalytic OER activity [11–13]. Moreover, the OER efficiencies of IrO_2 and/or RuO_2 (nanoparticle or nanodendrite) catalysts promoted on antimony-doped SnO_2 , which have revealed the high conductivities, have been reported by several groups [14,15]. Yet, in existing studies, the size microstructure of neither the supporting materials nor the noble-metal catalysts has been handled at the nano-size. The preparation method used for the nano-size affects their catalytic properties and morphology, including efficiency and durability [6,16,17].

Variations discovered in the performance of various IrO_2 nanomaterials have been presented due to the favorite of active sites on the surface [18]. Currently published reports that highlight the preparation of both IrO_2 and Ir thin films have been used in the layer deposition method of a single atom. However, this method required H_2 and O_3 gases [19–22]. Moreover, the set-up cost of the experimental system is high, and the deposition efficiency is low rate [19,20]. Additionally, the small size of metal and metal oxide nanoparticles needs to be investigated due to the chemical and electron properties of nanomaterial structures. In particular, various morphologies have been achieved by different experimental methods [16,23]. The nanoclusters of Ir metal and IrO_2 materials have drawn significant interest due to their conducting properties and favorite potential as electrocatalysts [24–27]. Especially, the Ir nanomaterials are also worthwhile considering in various applications, such as hydrogen evolution reactions. Therefore, to perform from the aforementioned advantages and expand their wide application, a deep understanding of the active sites on all kind of catalysts for electrochemical OER in acidic media is required [28–30].

For the stability of anode for OER in acid media, the metal oxide is more stable than the metal itself. If we can make metal oxides with hydroxyl groups of another metal oxide that is a supporter for anode electrode, the resulting covalently bonded metal–oxygen–metal oxide nanoparticles are expected to be stable. In addition, reduced metal oxide as a supporter should be better for the electrocatalyst since the reduced metal oxide is more conductive than metal oxide and also allows to use of a tiny amount.

Hence, synergetic advantages of covalently bonded Ir with hydroxyl groups of blue TiO_2 for OER in acidic conditions have been designed by using IrO_2 clusters decorated on reduced TiO_2 (blue TiO_2). This process produces Ir clusters (size of ~1 nm) that are loaded uniformly on the surface of blue TiO_2 that contribute to performance in the acidic OER. Furthermore, the covalently bonded IrO_2 –blue TiO_2 allows for higher mass activity due to the high fraction of available surface active sites, which reduces the required iridium nanocluster loading for electrolytic acidic OER. Our results illustrate that Ir(IV) atoms on the surface of blue TiO_2 ($\text{Ir}-\text{O}_2-2\text{Ti}$) can act as active sites, extend the active surface area, and enable a current density of 10 mA cm^{-2} at an overpotential of 342 mV, lower than IrO_2 of 438 mV in 0.1M HClO_4 electrolyte. Therefore, this work offers some insight into designing non-precious electrocatalytic OER in acidic media base on active sites and providing a flexible modulation strategy for developing real active sites.

2. Materials and Methods

2.1. Material Characterization

Sodium borohydride (NaBH_4) and Iridium(IV) chloride (IrCl_4) were purchased from Sigma-Aldrich company, Darmstadt, Germany. Structural characterization and morphology were carried out using a transmission electron microscope (TEM, JEOL 2100F, Tokyo, Japan) operated at 200 kV that is equipped to conduct HRTEM, HAADF-STEM images, and EDS elemental mapping. The TEM samples were prepared by slow evaporation of

dilute colloid in ethanol on a copper grid. The powder X-ray diffraction (XRD, Rigaku Ultima IV, USA) patterns were acquired to test the crystalline structure equipment at ambient condition with Cu κ 1 radiation. The elemental chemical composition of the as-prepared catalyst was confirmed by X-ray photoelectron spectroscopy (XPS, ESCA 2000, VG Microtech, UK) with MgK α as the X-ray source.

2.2. Synthesis of the IrO₂ Nanocluster-Doped Blue TiO₂ Nanoparticles

The IrO₂ nanocluster-doped blue TiO₂ nanoparticles were prepared using different ratios of IrCl₄ to blue TiO₂. An aqueous solution of the required amount of 0.1 M iridium (IV) chloride and 50 mg of blue TiO₂ was stirred in an ice bath, followed by the addition of a fresh, ice-cold, aqueous sodium borohydride (NaBH₄) solution. The molar ratio of the IrCl₄ precursor to NaBH₄ was maintained at 1:4. The color of the solution changed to pale yellow rapidly after starting the slow injection of borohydride. The temperature of the solution slowly reached ambient temperature as the solution was continuously stirred at room temperature for 48 h. During this process, the solution slowly changed to dark blue, indicating the formation of a colloid. The resulting solution was rinsed with DI water, adjusted to pH ~7 with HCl, continuously washed with ethanol and acetone several times, and then dried in a 70 °C vacuum oven for 1 h to yield a dark blue powder.

2.3. Electrochemical Measurements

We used an electrochemical workstation (VMP3, Biologic Science Instrument, France) to perform the electrocatalytic efficiency of the as-prepared catalysts. To arrange the working electrode, a mixture included of 5 mg catalyst, 0.18 mL isopropyl alcohol, 5 μ l of 5 wt% Nafion, and 0.33 mL of DI water, was dropped onto a glassy carbon electrode (mass loading of ~0.28 mg·cm⁻², a diameter of 3 mm) and drying overnight. The OER activity was tested in O₂-saturated 0.1 M HClO₄ at ambient condition using an electrochemical cell under a rotating disk electrode (RDE), obtained three electrodes: an Ag/AgCl electrode, a graphite rod and a glassy carbon electrode as the reference electrode, the counter electrode and working electrode, respectively. The LSV polarization curves were recorded at a scan rate of 5 mV s⁻¹, and all potentials were altered to refer to the reversible hydrogen electrode (RHE) by using the equation:

$$E_{\text{RHE}} = E_{\text{Ag/AgCl}} + E^0 + 0.059 \text{ pH (V)} \quad (1)$$

3. Results and Discussion

3.1. Structural Characterization

A schematic of the synthesis of IrO₂–blue TiO₂ NPs in the presence of NaBH₄ as a reducing reagent is shown in Figure 1a. The samples with different ratios of Ir⁴⁺ precursor to pure blue TiO₂ (BTO) are denoted as BI–10, BI–15, and BI–20. After the addition of NaBH₄, the formation of IrO₂ (101) on blue TiO₂ was verified by powder X-ray diffraction studies, which determines the peak position of 2 θ at 34.8°, as identified by standard ICSD #84577–IrO₂) [31,32], while all samples maintained the anatase peaks as in the original XRD blue TiO₂ nanoparticles (Figure 1b). Transmission electron microscopy (TEM) of the BI–15 NPs showed a nanostructure consisting of blue TiO₂ NPs (20–30 nm size) with uniform dots on the surface (Figure 1c). Furthermore, high-angle annular dark-field scanning transmission electron microscopy (HAADF-STEM) was checked to clearly confirm that the distribution and interconnection of IrO₂ clusters by the bright spots, with sizes between 1 and 2 nm on the blue TiO₂, [33,34], and energy-dispersive X-ray spectroscopy (EDS) elemental mapping results support the distribution of Ti, Ir, and O (Figure 1d). The Ir element detected on blue TiO₂ components is contacted on BI–15 NPs, and no significant impurities were detected.

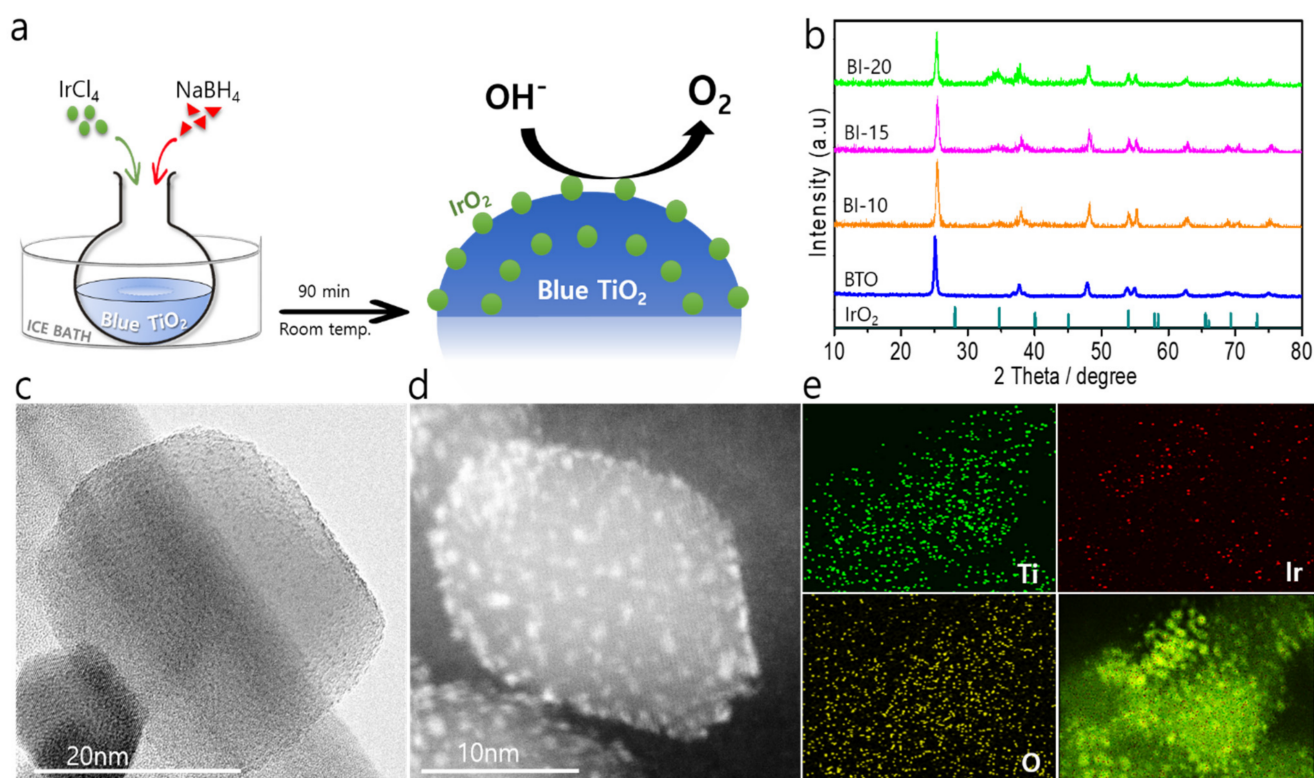


Figure 1. Synthesis and characterization of the IrO₂–blue TiO₂ NPs. (a) Schematic of the synthesis of IrO₂–Blue TiO₂NPs in the presence of NaBH₄ solution. (b) X-ray diffraction patterns of blue TiO₂ doped with different Ir wt%. (c) TEM images and (d) HRTEM image of the BI–15 catalyst. (e) EDS elemental maps of the BI–15 catalyst, showing the distribution of Ti, Ir and O.

To further confirm the chemical bond and oxidation states of the IrO₂–BTO NPs, the X-ray photoelectron spectroscopy (XPS) were employed to interrogate the presence of Ti 2p, Ir 4f, O 1s, and B 1s signatures (Figure 2).

Two broad peaks at 464.07 eV and 458.46 eV were observed, corresponding to the characteristic Ti 2p_{1/2} and Ti 2p_{3/2} Ti⁴⁺ peaks, respectively [10–35]. A smaller peak at 457.95 eV, characteristic of Ti³⁺, indicates the formation of Ti³⁺ on the surface of the BTO. However, the intensity of the Ti³⁺ peak decreased after IrO₂ loading on BTO, as seen in the IrO₂–BTO spectrum (Figure 2a) [2,13]. The broad binding energy band of Ir 4f was observed for both IrO₂–BTO and IrO₂ (Figure 2a,b) [36,37]. The band located at approximately 63.87 eV and 66.94 eV are demonstrated to the binding energy of Ir (IV) of IrO₂, and the band located at 62.32 eV and 65.67 eV are ascribed to the binding energy of Ir (III), which indicates the presence of multi-chemical states of Ir, including Ir (III) and Ir (IV) species in the oxidized zone [38]. In comparison to the spectra of the BTO sample, the Ti 2p and O 1s core-level XPS spectra of the BI–15 NPs (Figure 2a,c) showed a peak shift to higher binding energy (Ti 2p of 0.8 eV and O 1s of 0.9 eV), suggesting that Ir oxide species exist in the IrO₂–BTO NPs [38,39]. The presence of Ir oxide species in IrO₂–BTO may affect the shift to higher binding energy and result in shifting electron density toward the Ir in the Ir–O–Ti bonds at the interface of the BTO and IrO₂. Moreover, to confirm that the boron species were completely removed during the washing process, we acquired the B 1s XPS spectra of the BI-15 catalyst, which shows no peak associated with boron (Figure 2d).

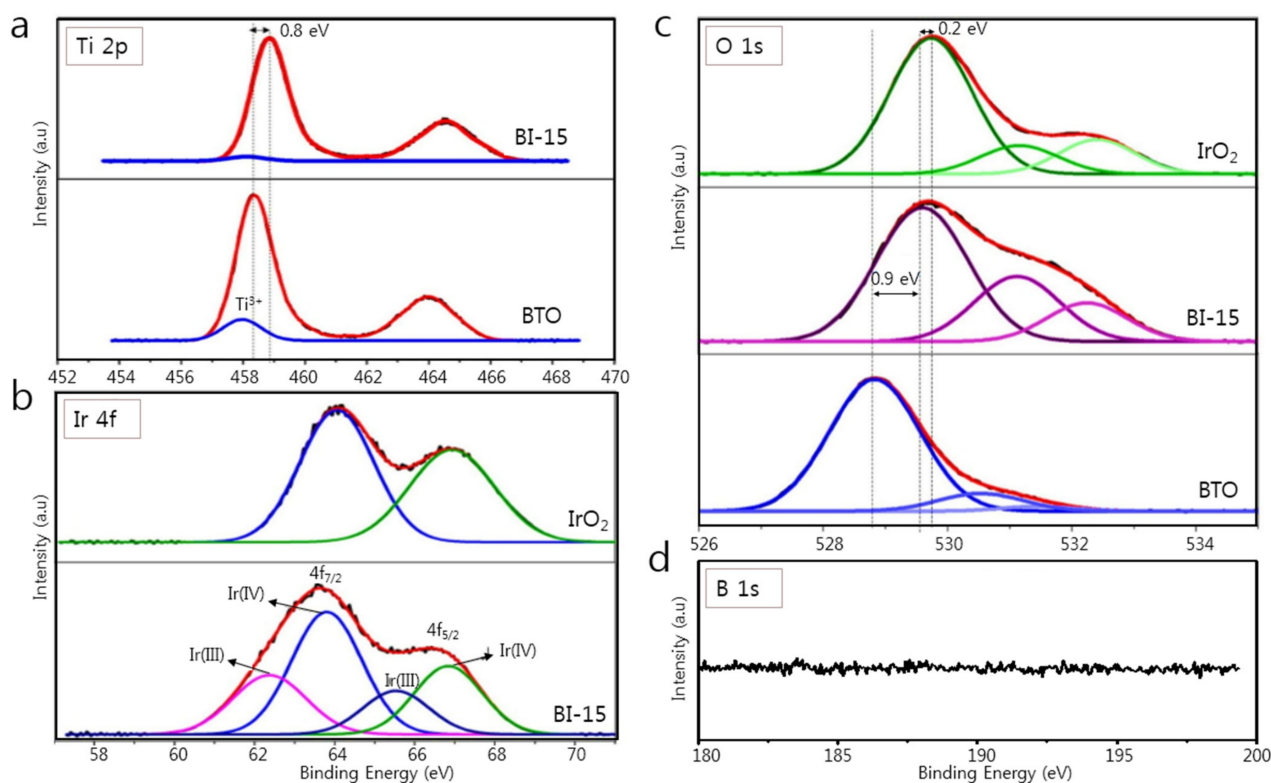


Figure 2. XPS analysis of BTO, IrO₂, and IrO₂-BTO samples: (a) Ti 2p spectra; (b) Ir 4f spectra, (c) O 1s spectra, and (d) B1s spectra.

3.2. Evaluation of OER Electrochemical Performance

Electrochemical characterization was performed to investigate the activities of the catalysts. We then continued to investigate the morphology-driven shifts in OER catalytic performance by evaluating the electrocatalytic activity in 0.1 M HClO₄ with an O₂-saturated state at ambient condition. Electrochemical impedance spectroscopy of all catalysts was recorded for iR correction before measuring. From the linear sweep voltammetry (LSV) curves (Figure 3a), the performance of the electrocatalyst for the OER was measured at a slow scan rate of 5 mV·s⁻¹ within the high anodic potential of 1.2–1.8 V vs. RHE after iR correction. All of the as-prepared catalysts with a RuO₂ as a point of reference electrocatalyst were tested. Among these samples, the BI-15 catalyst exposed the impressive OER efficiency with the lowest overpotential of 342 mV vs. RHE, which is even less than pure IrO₂ catalyst (445 mV), drive at the current density of 10 mA·cm⁻². Comparison of the overpotentials of various samples exhibited a relationship of BTO > BI-10 > IrO₂ > BI-20 > BI-15, suggesting that the IrO₂ species on BTO are active sites for electrocatalytic OER. Another possible explanation may be that due to the nucleophilicity that occurred on the Ir–O ligand, rapid O–O bond generation can explain for exceedingly enhanced OER efficiency of the IrO₂–BTO catalyst with a low kinetic barrier during electrocatalysis [40,41]. Moreover, on the Ir surface have referred the rich electron density due to strong interaction with the BTO (as shown in the XPS analysis spectra) also acts an important role in the promoted electrocatalytic effect of the BI-15 catalyst [41–43].

By using a small amount of Ir, achieving greatly efficient catalysis is a hardship for PEM electrolyzers. Therefore, we also evaluated the Ir mass activity (MA_{Ir}) of as-prepared catalysts based on the loading amounts of Ir, as shown in Figure 3b. The MA_{Ir} of the samples showed the relationship between IrO₂ < BI-10 < BI-20 < BI-15. The BI-15 has the greatest mass activity of 1.38 A/mg_{Ir}, which is almost 27 times higher than that of IrO₂, at an overpotential 350 mV. Notably, the BI-15 catalyst was similar to the BI-10 and BI-20 but 2.8 and 1.5 times the MA_{Ir}, respectively.

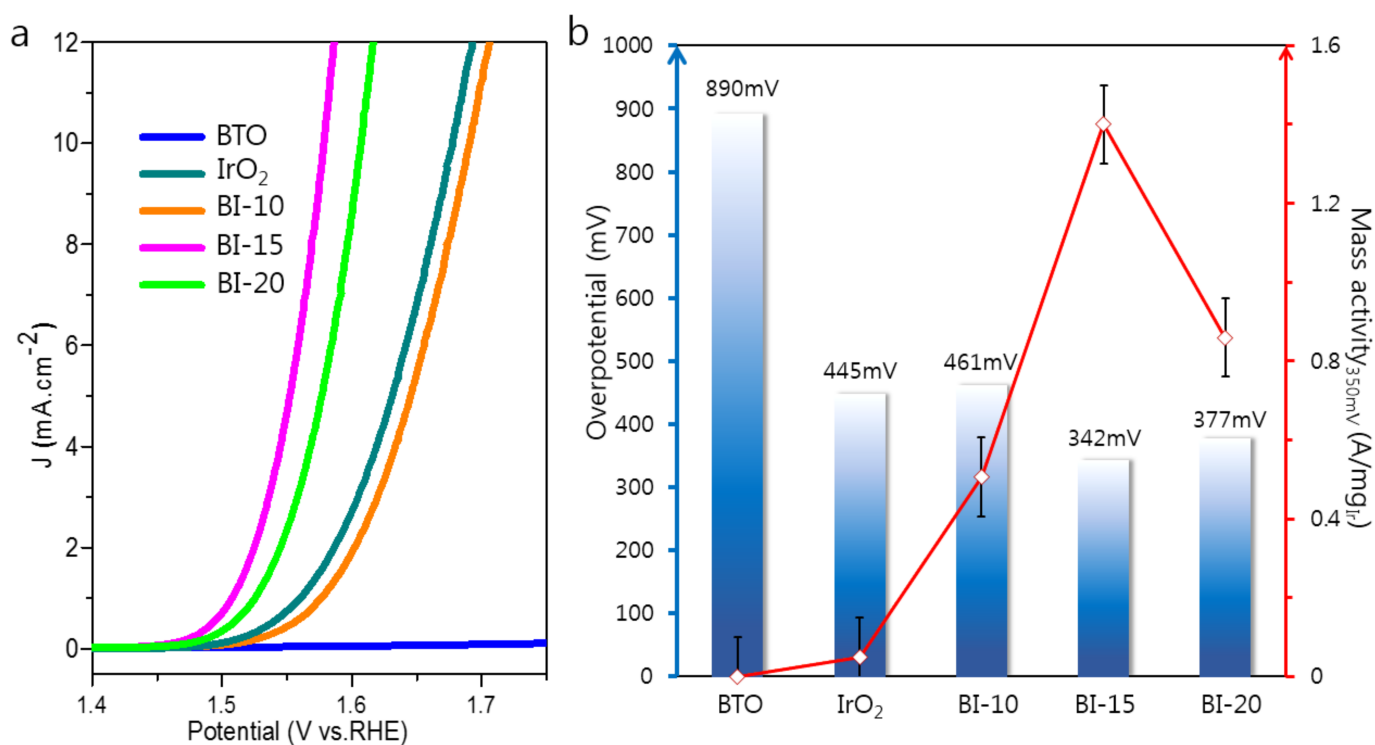


Figure 3. (a) LSV curves to evaluate OER activity, collected at the scan of 5 mV.s⁻¹ for BTO, IrO₂, BI-10, BI-15, and BI-20. (b) Bar graph showing required overpotentials to reach 10 mA cm⁻² and Ir mass activity at the overpotential of 350 mV (vs RHE) of various catalysts.

This difference arises mainly from the amount of Ir precursor during the synthesis process. The agglomeration of rich Ir precursors in BI-20 to form IrO₂ NPs with large size of 3–5 nm results in the loss of active sites during electrocatalytic OER (Figure S2) [41–44]. We further measured the efficiency of various catalysts by using Tafel plots (Figure 4a), which are evaluated by fitting the Tafel equation to the linear region of the plot of potential vs. $\log j$. In descending order, the Tafel slopes of pristine BTO, IrO₂, BI-10, BI-20, and BI-15, were 632.2, 114.3, 105.1, 81.7, and 68.2 mV.dec⁻¹, respectively, indicating that the BI-15 sample has the lowest Tafel slope, and therefore much higher OER kinetics for water oxidation [45,46].

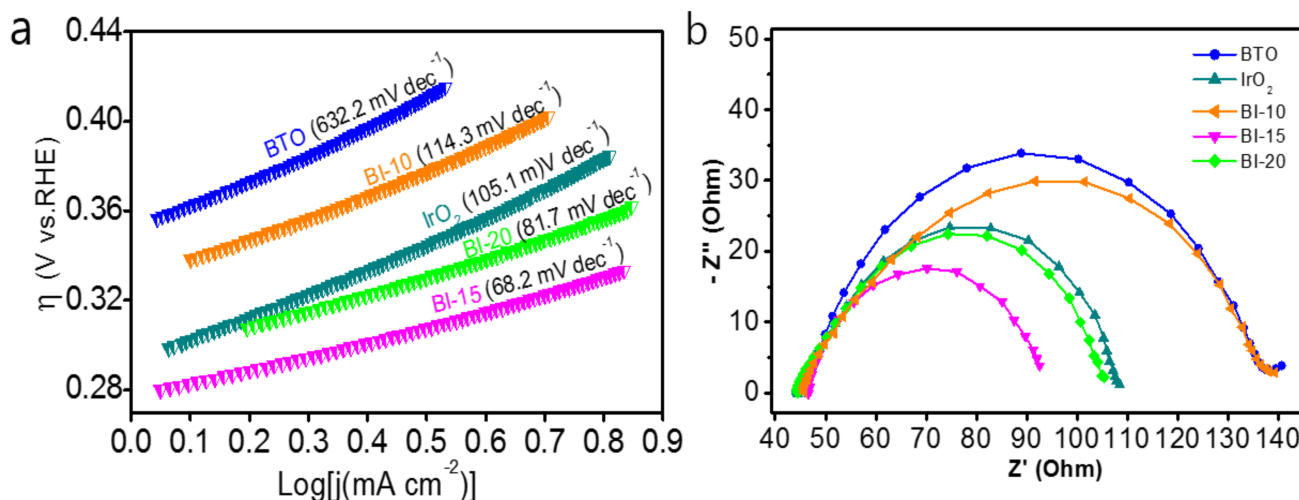


Figure 4. (a) Tafel slopes of BTO, IrO₂, BI-10, BI-15, and BI-20 electrodes. (b) Electrochemical impedance spectrogram of BTO, IrO₂, BI-10, BI-15, and BI-20 electrodes at the potential of 1.27 V, conducted before OER testing.

In more detail, as indicated by XPS spectral (Figure 2), we proposed the pathway of the interconnection between the IrO_2 nanocluster and blue TiO_2 nanoparticles to form the covalently Ir(IV) bond on conducted blue TiO_2 (Figure 5). NaBH_4 played an important role in the synthesis of IrO_2 /BTO NPs, which de-protonated hydrogen to give an oxygen anion, leading to IrCl_4 to form $\text{Ir}-\text{O}_2-2\text{Ti}$ [16].

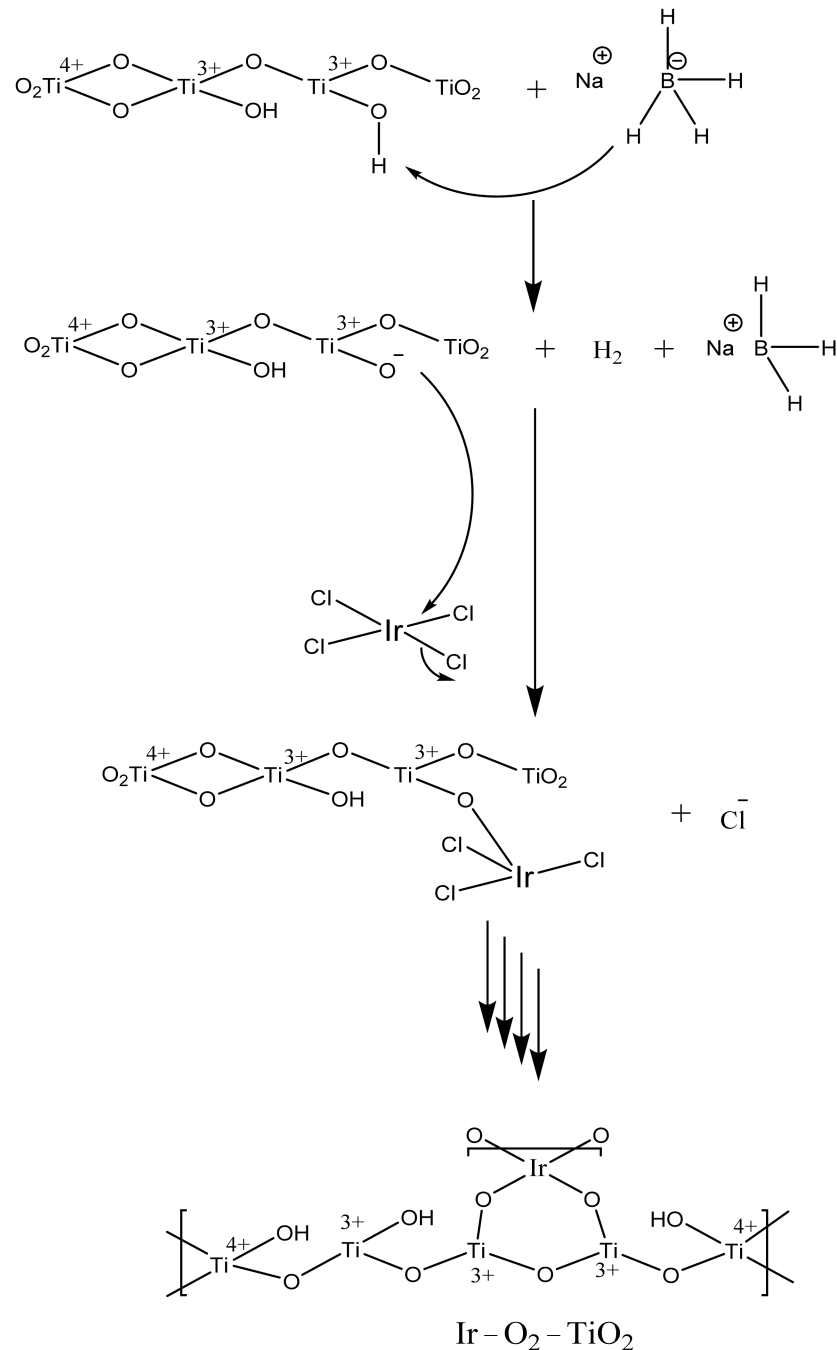


Figure 5. Growth schematic illustrate a covalently bonding of Ir on blue TiO_2 nanostructure.

Finally, the stability of the BI-15 catalyst was tested utilizing chronoamperometry at a potential of 1.54 V and a current density of $10 \text{ mA}\cdot\text{cm}^{-2}$ in acidic conditions for 120 min (Figure S5). A slight enhancement in potential over this time gap was observed, which shows poor durability with sharp degradation during measuring catalysis (Figure S4).

4. Conclusions

Overall, this study demonstrated a feasible method to modify the surface of blue TiO₂ nanoparticles with IrO₂ nanoclusters (size of ~1 nm) (Ir–O₂–2Ti NPs) in the presence of borohydride as a reducing agent at room temperature. We evaluated the morphology-driven shift in OER catalytic efficiency of the IrO₂–BTO NPs, which BTO using as a supported catalyst, to understand how to tune catalytic performance. The IrO₂–BTO NP catalyst exhibited superior catalytic activity (overpotential of 342 mV at 10 mA cm^{−2}) and the greatest mass activity at 1.38 A/mg_{Ir}, which is almost 27 times higher than that of IrO₂ alone, at the 350 mV in 0.1 M HClO₄. Moreover, the mass activity of this catalyst substantially exceeds those of state-of-the-art IrO₂ support catalysts. Our work opens new avenues to constructing advanced electrocatalysts based on novel catalysts structures that can help develop more active OER catalysts for acidic conditions.

Supplementary Materials: The following are available online at <https://www.mdpi.com/article/10.3390/catal11101176/s1>, Figure S1: The Brunauer-Emmett-Teller (BET) surface area of IrO₂ and BI-15 samples, Figure S2: TEM images showed a different size of IrO₂ on the BI-10 and BI-20 samples, Figure S3: Comparison of LSV curves of P25, BTO, IrO₂, PI-15 and BI-15 collected at the scan of 5 mV·s^{−1} in 0.1 M HClO₄ electrolyte, Figure S4: TEM image of BI-15 after 120 min electrocatalytic OER in 0.1 M HClO₄, Figure S5: Acid stability test of BI-15 catalyst in 0.1 M HClO₄ electrolyte using chronoamperometry at a potential 1.54 V and a current density of 10 mA·cm^{−2}.

Author Contributions: Design and performance of the experiments, C.T.K.N.; analysis of the experimental data, N.Q.T.; contribution for XRD analysis, T.A.L.; writing of the manuscript, C.T.K.N.; revision and edition of the manuscript, H.L. All authors have read and agreed to the published version of the manuscript.

Funding: This work was supported by the Institute for Basic Science (IBS-R011-D1). This work was partially supported by the Korea Evaluation Institute of Industrial Technology (20004627) and the INNOPOLIS Foundation (2019-DD-SB-0602).

Data Availability Statement: The data presented in this study are available on request from the corresponding author.

Conflicts of Interest: The authors declare no conflict of interest.

References

1. Ahicart, M.B.; López, J.S.; Carbó, J.J.; Poblet, J.M.; Mascaros, J.R.G. Polyoxometalate electrocatalysts based on earth-abundant metals for efficient water oxidation in acidic media. *Nat. Chem.* **2018**, *10*, 24–30. [[CrossRef](#)] [[PubMed](#)]
2. Nguyen, C.T.K.; Tran, N.Q.; Seo, S.; Hwang, H.; Oh, S.; Yu, J.; Lee, J.; Le, T.A.; Hwang, J.; Kim, M.; et al. Highly efficient nanostructured metal-decorated hybrid semiconductors for solar conversion of CO₂ with almost complete CO selectivity. *Mater. Today* **2019**, *35*, 25–33. [[CrossRef](#)]
3. Tran, N.Q.; Le, T.A.; Kim, H.; Hong, Y.; Cho, Y.; Park, G.H.; Kim, H.; Kim, M.; Lee, J.; Yoo, W.S.; et al. Low Iridium Content Confined inside a Co₃O₄ Hollow Sphere for Superior Acidic Water Oxidation. *ACS Sustain. Chem. Eng.* **2019**, *7*, 16640–16650. [[CrossRef](#)]
4. Yu, J.; Seo, S.; Luo, Y.; Sun, Y.; Oh, S.; Nguyen, C.T.K.; Seo, C.; Kim, J.H.; Kim, J.; Lee, H. Efficient and Stable Solar Hydrogen Generation of Hydrophilic Rhenium-Disulfide-Based Photocatalysts via Chemically Controlled Charge Transfer Paths. *ACS Nano* **2020**, *14*, 1715–1726. [[CrossRef](#)]
5. Gu, X.K.; Camayang, J.C.A.; Samira, S.; Nikolla, E. Oxygen evolution electrocatalysis using mixed metal oxides under acidic conditions: Challenges and opportunities. *J. Catal.* **2020**, *388*, 130–140. [[CrossRef](#)]
6. Kumar, S., S.; Himabindu., V. Hydrogen production by PEM water electrolysis – A review. *Mater. Sci. Energy Technol.* **2019**, *2*, 442–454.
7. Chandrasekaran, S.; Ma, D.; Ge, Y.; Deng, L.; Bowen, C.; Roscow, J.; Zhang, Y.; Lin, Z.; Misra, R.D.K.; Li, J.; et al. Electronic structure engineering on two-dimensional (2D) electrocatalytic materials for oxygen reduction, oxygen evolution, and hydrogen evolution reactions. *Nano Energy* **2020**, *77*, 105080. [[CrossRef](#)]
8. Shi, Q.; Zhu, C.; Du, D.; Lin, Y. Robust noble metal-based electrocatalysts for oxygen evolution reaction. *Chem. Soc. Rev.* **2019**, *48*, 3181–3192. [[CrossRef](#)]
9. Alia, S.M.; Shulda, S.; Ngo, C.; Pylypenko, S.; Pivovar, B.S. Iridium-Based Nanowires as Highly Active, Oxygen Evolution Reaction Electrocatalysts. *ACS Catal.* **2018**, *8*, 2111–2120. [[CrossRef](#)]

10. Oakton, E.; Lebedev, D.; Povia, M.; Abbott, D.F.; Fabbri, E.; Fedorov, A.; Nachtegaal, M.; Coperet, C.; Schmidt, T.J. IrO₂-TiO₂: A High-Surface-Area, Active, and Stable Electrocatalyst for the Oxygen Evolution Reaction. *ACS Catal.* **2017**, *7*, 2346–2352. [[CrossRef](#)]
11. Cheng, J.; Yang, J.; Kitano, S.; Juhasz, G.; Higashi, M.; Sadakiyo, M.; Kato, K.; Yoshioka, S.; Sugiyama, T.; Yamauchi, M.; et al. Impact of Ir-Valence Control and Surface Nanostructure on Oxygen Evolution Reaction over a Highly Efficient Ir-TiO₂ Nanorod Catalyst. *ACS Catal.* **2019**, *9*, 6974–6986. [[CrossRef](#)]
12. Kwon, T.; Hwang, H.; Sa, Y.J.; Park, J.; Baik, H.; Joo, S.H.; Lee, K. Cobalt Assisted Synthesis of IrCu Hollow Octahedral Nanocages as Highly Active Electrocatalysts toward Oxygen Evolution Reaction. *Adv. Funct. Mater.* **2017**, *27*, 1604688. [[CrossRef](#)]
13. Zhang, K.; Wang, L.; Kim, J.K.; Ma, M.; Veerappan, G.; Lee, C.L.; Kong, K.J.; Lee, H.; Park, J.H. An order/disorder/water junction system for highly efficient co-catalyst-free photocatalytic hydrogen generation. *Energy Environ. Sci.* **2016**, *9*, 499. [[CrossRef](#)]
14. Yang, L.; Yu, G.; Ai, X.; Yan, W.; Duan, H.; Chen, W.; Li, X.; Wang, T.; Zhang, C.; Huang, X.; et al. Efficient oxygen evolution electrocatalysis in acid by a perovskite with face-sharing IrO₆ octahedral dimers. *Nat. Commun.* **2018**, *9*, 5236. [[CrossRef](#)]
15. Park, J.; Sa, Y.J.; Baik, H.; Kwon, T.; Joo, S.H.; Lee, K. Iridium-Based Multimetallic Nanoframe@Nanoframe Structure: An Efficient and Robust Electrocatalyst toward Oxygen Evolution Reaction. *ACS Nano* **2017**, *11*, 5500–5509. [[CrossRef](#)]
16. Chakrapani, K.; Sampath, S. The dual role of borohydride depending on reaction temperature: Synthesis of iridium and iridium oxide. *Chem. Commun.* **2015**, *51*, 9690. [[CrossRef](#)]
17. Tachikawa, T.; Beniya, A.; Shigetoh, K.; Higashi, S. Relationship between OER Activity and Annealing Temperature of Sputter-Deposited Flat IrO₂ Thin Films. *Catal. Lett.* **2020**, *150*, 1976–1984. [[CrossRef](#)]
18. Seitz, L.C.; Dickens, C.F.; Nishio, K.; Hikita, Y.; Montoya, J.; Doyle, A.; Kirk, C.; Vojvodic, A.; Hwang, H.Y.; Norskov, J.K.; et al. A highly active and stable IrO_x/SrIrO₃ catalyst for the oxygen evolution reaction. *Science* **2016**, *353*, 1011–1014. [[CrossRef](#)]
19. Mattinen, M.; Hämäläinen, J.; Vehkamäki, M.; Heikkilä, M.J.; Mizohata, K.; Jalkanen, P.; Räisänen, J.; Ritala, M.; Leskelä, M. Atomic Layer Deposition of Iridium Thin Films Using Sequential Oxygen and Hydrogen Pulses. *J. Phys. Chem. C* **2016**, *28*, 15235–15243. [[CrossRef](#)]
20. Matienzo, D.D.; Settipani, D.; Instuli, E.; Kallio, T. Active IrO₂ and NiO Thin Films Prepared by Atomic Layer Deposition for Oxygen Evolution Reaction. *Catalysts* **2020**, *10*, 92. [[CrossRef](#)]
21. Anantharaj, S.; Karthick, K.; Kundu, S. Evolution of layered double hydroxides (LDH) as high performance water oxidation electrocatalysts: A review with insights on structure, activity and mechanism. *Mater. Today Energy* **2017**, *6*, 1–26. [[CrossRef](#)]
22. Mattinen, M.; Hämäläinen, J.; Gao, F.; Jalkanen, P.; Mizohata, K.; Räisänen, J.; Puurunen, R.L.; Ritala, M.; Leskelä, M. Nucleation and Conformality of Iridium and Iridium Oxide Thin Films Grown by Atomic Layer Deposition. *Langmuir* **2016**, *32*, 10559–10569. [[CrossRef](#)] [[PubMed](#)]
23. Lettenmeier, P.; Majchel, J.; Wang, L.; Saveleva, V.A.; Zafeiratos, S.; Savinova, E.R.; Gallet, J.J.; Bournel, F.; Gago, A.S.; Friedrich, K.A. Highly active nano-sized iridium catalysts: Synthesis and operando spectroscopy in a proton exchange membrane electrolyzer. *Chem. Sci.* **2018**, *9*, 3570–3579. [[CrossRef](#)] [[PubMed](#)]
24. Jiang, K.; Luo, M.; Peng, M.; Yu, Y.; Lu, Y.R.; Chan, T.S.; Liu, P.; Groot, F.M.F.; Tan, Y. Dynamic active-site generation of atomic iridium stabilized on nanoporous metal phosphides for water oxidation. *Nat. Commun.* **2020**, *11*, 2701. [[CrossRef](#)]
25. Li, C.; Baek, J.B. Recent Advances in Noble Metal (Pt, Ru, and Ir)-Based Electrocatalysts for Efficient Hydrogen Evolution Reaction. *ACS Omega* **2020**, *5*, 31–40. [[CrossRef](#)]
26. Cho, Y.; Le, T.A.; Lee, H. Understanding Surface Modulation to Improve the Photo/Electrocatalysts for Water Oxidation/Reduction. *Molecules* **2020**, *25*, 1965. [[CrossRef](#)]
27. Tahir, M.; Pan, L.; Idrees, F.; Zhang, X.; Wang, L.; Zou, J.J.; Wang, Z.L. Electrocatalytic oxygen evolution reaction for energy conversion and storage: A comprehensive review. *Nano Energy* **2017**, *37*, 136–157. [[CrossRef](#)]
28. Reier, T.; Nong, H.N.; Teschner, D.; Schlögl, R.; Strasser, P. Electrocatalytic Oxygen Evolution Reaction in Acidic Environments – Reaction Mechanisms and Catalysts. *Adv. Energy Mater.* **2017**, *7*, 1601275. [[CrossRef](#)]
29. Tong, J.; Liu, Y.; Peng, Q.; Hu, W.; Wu, Q. An efficient Sb-SnO₂-supported IrO₂ electrocatalyst for the oxygen evolution reaction in acidic medium. *J. Mater. Sci.* **2017**, *52*, 13427–13443. [[CrossRef](#)]
30. Kim, Y.T.; Lopes, P.P.; Park, S.A.; Lee, A.Y.; Lim, J.; Lee, H.; Back, S.; Jung, Y.; Danilovic, N.; Stamenkovic, V.; et al. Balancing activity, stability and conductivity of nanoporous core-shell iridium/iridium oxide oxygen evolution catalysts. *Nat. Commun.* **2017**, *8*, 1449. [[CrossRef](#)]
31. Hwang, H.M.; Oh, S.; Shim, J.H.; Kim, Y.M.; Kim, A.; Kim, D.; Kim, J.; Bak, S.; Cho, Y.; Bui, V.Q.; et al. Phase-Selective Disordered Anatase/Ordered Rutile Interface System for Visible-Light-Driven, Metal-Free CO₂ Reduction. *ACS Appl. Mater. Interfaces* **2019**, *11*, 35693–35701. [[CrossRef](#)]
32. Povia, M.; Abbott, D.F.; Herranz, J.; Heinritz, A.; Lebedev, D.; Kim, B.J.; Fabbri, E.; Patru, A.; Kohlbrecher, J.; Schaublin, R.; et al. Operando X-ray characterization of high surface area iridium oxides to decouple their activity losses for the oxygen evolution reaction. *Energy Environ. Sci.* **2019**, *12*, 3038–3052. [[CrossRef](#)]
33. Halder, A.; Liu, C.; Liu, Z.; Emery, J.D.; Pellin, M.J.; Curtiss, L.A.; Zapol, P.; Vajda, S.; Martinson, A.B.F. Water Oxidation Catalysis via Size-Selected Iridium Clusters. *J. Phys. Chem. C* **2018**, *122*, 9965–9972. [[CrossRef](#)]
34. Chen, L.W.; Tong, L.; Nan, H.; Chu, S.Q.; Liang, H.W. Sub-2 nm Ir Nanoclusters Immobilized on Mesoporous Nitrogen-Doped Carbons as Efficient Catalysts for Selective Hydrogenation. *ACS Appl. Nano Mater.* **2019**, *10*, 6546–6553. [[CrossRef](#)]

35. Meekins, B.H.; Kamat, P.V. Role of Water Oxidation Catalyst IrO₂ in Shuttling Photogenerated Holes Across TiO₂ Interface. *J. Phys. Chem. Lett.* **2011**, *18*, 2304–2310. [[CrossRef](#)]
36. Pham, C.V.; Bühler, M.; Knöppel, J.; Bierling, M.; Seeberger, D.; López, D.E.; Mayrhofer, K.J.J.; Cherevko, S.; Thiele, S. IrO₂ coated TiO₂ core-shell microparticles advance performance of low loading proton exchange membrane water electrolyzers. *Appl. Catal. B Environ.* **2020**, *269*, 118762. [[CrossRef](#)]
37. Yuan, M.; Zhu, Y.; Deng, L.; Ming, R.; Zhang, A.; Li, W.; Chaia, B.; Ren, Z. IrO₂-TiO₂ electrocatalysts for the hydrogen evolution reaction in acidic water electrolysis without activation. *New J. Chem.* **2017**, *41*, 6152–6159. [[CrossRef](#)]
38. Zhong, W.; Lin, Z.; Feng, S.; Wang, D.; Shen, S.; Zhang, Q.; Gu, L.; Wang, Z.; Fang, B. Improved oxygen evolution activity of IrO₂ by in situ engineering of an ultra-small Ir sphere shell utilizing a pulsed laser. *Nanoscale* **2019**, *11*, 4407–4413. [[CrossRef](#)]
39. Ohno, H.; Nohara, S.; Kakinuma, K.; Uchida, M.; Uchida, H. Effect of Electronic Conductivities of Iridium Oxide/Doped SnO₂ Oxygen-Evolving Catalysts on the Polarization Properties in Proton Exchange Membrane Water Electrolysis. *Catalysts* **2019**, *9*, 74. [[CrossRef](#)]
40. Grimaud, A.; Demortière, A.; Saubanière, M.; Dachraoui, W.; Duchamp, M.; Doublet, M.L.; Tarascon, J.M. Activation of surface oxygen sites on an iridium-based model catalyst for the oxygen evolution reaction. *Nat. Energy* **2016**, *2*, 16189. [[CrossRef](#)]
41. Smith, R.D.L.; Sporinova, B.; Fagan, R.D.; Trudel, S.; Berlinguette, C.P. Facile Photochemical Preparation of Amorphous Iridium Oxide Films for Water Oxidation Catalysis. *Chem. Mater.* **2014**, *26*, 1654–1659. [[CrossRef](#)]
42. Wua, X.; Fenga, B.; Lia, W.; Niua, Y.; Yua, Y.; Lua, S.; Zhonga, C.; Liuc, P.; Tianc, Z.; Chenc, L.; et al. Metal-support interaction boosted electrocatalysis of ultrasmall iridium nanoparticles supported on nitrogen doped graphene for highly efficient water electrolysis in acidic and alkaline media. *Nano Energy* **2019**, *62*, 117–126. [[CrossRef](#)]
43. Gorlin, Y.; Chung, C.J.; Benck, J.D.; Nordlund, D.; Seitz, L.; Weng, T.C.; Sokaras, D.; Clemens, B.M.; Jaramillo, T.F. Understanding Interactions between Manganese Oxide and Gold That Lead to Enhanced Activity for Electrocatalytic Water Oxidation. *J. Am. Chem. Soc.* **2014**, *136*, 4920–4926. [[CrossRef](#)] [[PubMed](#)]
44. Lyons, M.E.G.; Floquet, S. Mechanism of oxygen reactions at porous oxide electrodes. Part 2—Oxygen evolution at RuO₂, IrO₂ and Ir_xRu_{1-x}O₂ electrodes in aqueous acid and alkaline solution. *Phys. Chem. Chem. Phys.* **2011**, *13*, 5314–5335. [[CrossRef](#)] [[PubMed](#)]
45. Zhang, R.; Dubouis, N.; Osman, M.B.; Yin, W.; Sougrati, M.T.; Corte, D.A.D.; Giaume, D.; Grimaud, A. A Dissolution/Precipitation Equilibrium on the Surface of Iridium-Based Perovskites Controls Their Activity as Oxygen Evolution Reaction Catalysts in Acidic Media. *Angew. Chem. Int. Ed.* **2019**, *58*, 4571–4575. [[CrossRef](#)] [[PubMed](#)]
46. Nong, H.N.; Reier, T.; Oh, H.S.; Gliech, M.; Paciok, P.; Vu, T.H.T.; Teschner, D.; Heggen, M.; Petkov, V.; Schlögl, R.; et al. A unique oxygen ligand environment facilitates water oxidation in hole-doped IrNiO_x core-shell electrocatalysts. *Nat. Catal.* **2018**, *1*, 841–851. [[CrossRef](#)]